Nanoscale

Accepted Manuscript

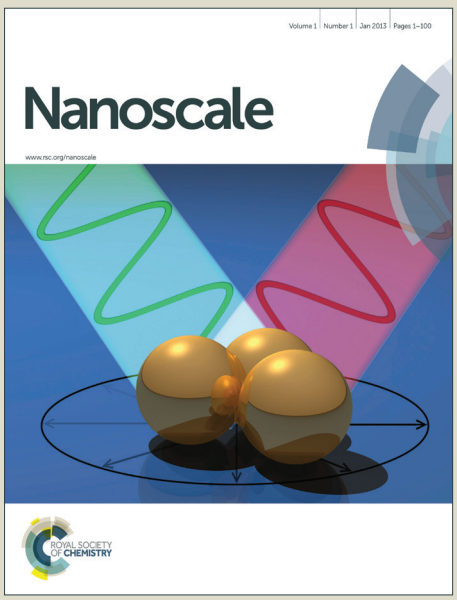

ROYAL SOCIETY OF CHEMISTRY

www.rsc.org/nanoscale

Journal Name

RSCPublishing

ARTICLE

Highly Efficient and Bendable Organic Solar Cells Using a Three-Dimensional Transparent Conducting Electrode

Cite this: DOI: 10.1039/x0xx00000x

Received 00th January 2012,
Accepted 00th January 2012

DOI: 10.1039/x0xx00000x

www.rsc.org/

Wei Wang,[a,b] Tae-Sung Bae,[c] Yeon Hyun Park,[b] Dong Ho Kim,[b] Sunghun Lee,[b] Guanghui Min,[a] Gun-Hwan Lee,[b] Myung-Kwan Song,*[b] and Jungheum Yun*[b]

A three-dimensional (3D) transparent conducting electrode, consisting of a quasi-periodic array of discrete indium-tin-oxide (ITO) nanoparticles superimposed on a highly conducting oxide–metal–oxide multilayer using ITO and silver oxide (AgO_x) as oxide and metal, respectively, is synthesized on a polymer substrate and used as anode in highly flexible organic solar cells (OSCs). The 3D electrode is fabricated using vacuum sputtering sequences to achieve self-assembly of distinct ITO nanoparticles on a continuous ITO–AgO_x–ITO multilayer at room-temperature without applying conventional high-temperature vapour–liquid–solid growth, solution-based nanoparticle coating, or complicated nanopatterning techniques. Since the 3D electrode enhances the hole-extraction rate in OSCs owing to its high surface area and low effective series resistance for hole transport, OSCs based on this 3D electrode exhibit a power conversion efficiency that is 11−22% higher than that achievable in OSCs by means of conventional planar ITO film-type electrodes. A record high efficiency of 6.74% can be achieved in a bendable OSC fabricated on a poly (ethylene terephthalate) substrate.

Introduction

Organic solar cells (OSCs) have received significant attention owing to their low cost and large-area fabrication.[1,2] However, their power conversion efficiencies (PCEs) are still significantly lower than those of conventional inorganic solar cells, which commonly exhibit PCEs of over 10%. The main reason for this drawback is the low carrier mobility of the semiconducting photoactive polymers used for the fabrication of OSCs. In an OSC, free charge carriers have to be transported through a semiconducting polymer to electrodes to achieve an efficient charge separation; however, significant current losses occur in such OSCs owing to charge recombination.[1] One solution to prevent the poor charge separation in OSCs is to provide a direct and ordered charge-transport path by combining the polymer with nanostructured, transparent conducting oxide (TCO) electrodes.[3,4] This can be achieved by using vertically oriented three-dimensional (3D) nanostructured TCO electrodes that are either template-based porous nanostructures[5–8] or free-standing nanorods.[9–14] Compared with 1D nanostructures of similar materials, 3D TCO nanostructured electrodes exhibit improved charge transport and, thus, enhanced photocurrent collection because of their larger surface areas and their ability to act as direct charge-transport pathways.[15–17] Furthermore, the interference of incident light in 3D TCO nanostructures leads to a reduced reflection and increased scattering of the incident light within the nanostructures, thereby improving the photon absorption by the photoactive polymer owing to the increase in the intensity and path length of the incident photons. These desirable characteristics of 3D TCO nanostructured electrodes, which result in boosts in charge generation, transport, and collection efficiency, have therefore induced their use for improving the PCE values of OSCs.

However, 3D TCO nanostructured electrodes are being used primarily in OSCs that are fabricated on glass substrates which are not mechanically flexible. No effective solution has yet been found to allow for the fabrication of highly efficient 3D TCO electrodes on flexible, heat-sensitive polymer substrates owing to the fact that the fabrication of conventional 3D TCO electrodes involves high temperatures. High-aspect-ratio TCO

nanorods are most commonly grown by vapour–liquid–solid (VLS) growth-based techniques.[18] These include vapour-phase-growth methods such as vapour transport growth,[19,20] molecular beam epitaxy,[21] and pulsed laser deposition,[22] all of which normally involve growth temperatures above 500 °C.[23] However, nanorod growth by means of these high-temperature methods is often accompanied by the development of abnormally tall nanorods, which can cause significant leakage currents, implying a degradation of the OSC performance. Yu et al.[14,24] recently fabricated 3D nanorods of indium tin oxide (ITO) at relatively low temperatures by electron beam evaporation using self-catalytic indium-tin nanodots. However, the ITO nanorods still require a growth temperature of more than 200 °C for exhibiting appropriate electrical conductivities and optical transparencies to act as front electrodes of OSCs. This temperature by far exceeds the glass transition temperatures of most heat-sensitive polymer substrates, which are normally lower than 100 °C. On the other hand, solution-based coating methods including electrospinning,[25] sol–gel,[26] and electrophoretic deposition[27] typically involve lower growth temperatures than in case of the abovementioned vapour-phase-growth methods.[23] However, solution-grown TCO nanostructures are not suitable for being electrodes of OSCs because they exhibit electrical resistivities that are often four, or even more, orders of magnitude higher than those of vapour-deposited TCO nanostructured electrodes, whose resistivities are in the range of 10^{-4} Ω·cm.[23,27]

The aim of this study was to fabricate an efficient 3D transparent conducting electrode for use in bendable OSCs, fabricated on heat-sensitive polymer substrates. We report that this task was readily achieved by fabricating a hybrid nanostructure, which consisted of an ITO nanoparticle array (NPA) superimposed on a continuous ITO–silver oxide (AgO_x)–ITO (IAOI) multilayer on top of a flexible polyethylene terephthalate (PET) substrate, by a room-temperature sputtering process. No high-temperature vapour–liquid–solid or post-deposition sintering processes were required for the synthesis of the electrode. The use of this self-assembled 3D electrode acting as anode in OSCs enhanced the charge transport and separation efficiencies of the devices, owing to its large surface area and low effective series resistance for hole transport. The PCE of the 3D electrode-based OSCs was 11–22% higher than that of devices based on conventional ITO film-type electrodes. As a result, a PCE of 6.74% was achieved, corresponding to a record high value for polymer-based OSCs and comparable to that of OSCs fabricated on glass substrates. A bulk heterojunction coating of poly[[4,8-bis[(2-ethylhexyl)oxy]benzo[1,2-b:4,5-b']dithiophene-2,6-diyl][3-fluoro-2-[(2-ethylhexyl)carbonyl]thieno[3,4-b]thiophenediyl]] (PTB7):[6,6]-phenyl-C_{71}-butyric acid methyl ester ($PC_{71}BM$) on top of the 3D electrode was used as photoactive layer. Furthermore, the 3D electrode exhibited excellent electrical and structural stability, even when the polymer substrates were subject to extreme bending. This allows for the production of completely foldable OSCs.

Experimental section

Electrode fabrication and characterization. The IAOI-NPA electrode was fabricated on 75-μm-thick PET substrates (Panac Co. Ltd.), which were coated with an 8-μm-thick acrylate layer composed of thermally cross-linked poly(acrylic acid) species. First, the PET substrate was subjected to a plasma-induced pre-treatment and, then, the IAOI multilayer and the ITO NPA were deposited via sputtering at room temperature. The pre-treatment was performed using a custom-built plasma-enhanced chemical vapour deposition (PECVD) system which employed a capacitively coupled radio-frequency (RF) plasma supply at 13.56 MHz. The PET substrate was attached to the plate electrode, which was 6 inches in diameter, and the chamber was evacuated to a base pressure of 6.7 Pa. The PET surface was exposed to an Ar plasma that was produced using an RF power of 200 W (1.1 W Ω^{-1}) at a working pressure of 22.7 Pa. Several pre-treatment times were investigated. Next, the IAOI multilayer was deposited on the pre-treated PET surface using a magnetron multi-gun sputtering system (A-Tech System Co., Ltd., Flexlab system 100) at room temperature. The substrate was placed at a distance of approximately 15 cm from the Ag and ITO targets. The IAOI multilayer and, subsequently, the ITO NPA depositions on the plasma-pre-treated PET surface were performed while maintaining vacuum conditions. The bottom and top ITO layers were deposited using a 4-inch ITO (10 wt% Sn-doped In_2O_3) target (99.999%, Advanced Nano Products Co. Ltd.) at an RF power of 200 W (0.53 W cm^{-2}) and a working pressure of 0.4 Pa. The pressure was maintained by introducing Ar gas (99.9999%) at a flow rate of 60 sccm. Thin Ag and AgO_x layers with different O/Ag atomic ratios were deposited on the bottom ITO layer using the same system for a reactive direct current (dc) sputtering process. A 4-inch Ag target (Williams Advanced Materials Inc.) was employed for this purpose. The working pressure and dc power were set at 0.4 Pa and 50 W (0.13 W cm^{-2}), respectively. The Ag layer was deposited by introducing pure Ar at a flow rate of 45 sccm, whereas the AgO_x layers were deposited by introducing a gas mixture comprising Ar (at a flow rate of 45 sccm) and O_2 (at a flow rate of 2–24 sccm).

Plane and cross-sectional images of the 3D IAOI-NPA and planar ITO film-type electrodes were obtained using ultrahigh-resolution (UHR) field-emission scanning electron microscopy (FE-SEM, Hitachi: S-5500) at the Korea Basic Science Institute (Jeonju, South Korea). An electron beam with a relatively low accelerating voltage (2–5 kV) was used in order to avoid thermal damage of the delicate surface of the PET surface. The cross-sectional structure and chemical composition of the IAOI-NPA electrodes were determined using scanning transmission electron microscopy (STEM, FEI: Titan) and energy-dispersive X-ray spectroscopy (EDS) at the Korea Institute of Science and Technology (Seoul, South Korea). The O/Ag atomic ratios of the AgO_x layers, which were deposited using different O_2 flow rates, were determined using X-ray photoelectron spectroscopy (XPS, VG Scientific: Escalab 200R), which was performed using an Al K_α (1486.6 eV) X-ray

source at 250 W (12.5 kV and 20 mA) and a concentric hemispherical analyzer operated at a scan pass energy of 100 eV, at the Electronic and Telecommunications Research Institute (Daejeon, South Korea). The crystallographic characteristics of the embedded Ag and AgO_x layers, which had a thickness of 80 nm, were determined for an angular range (2θ) of 30–70° using grazing incidence (GI) X-ray diffraction (GI-XRD, PANalytical: Empyrean) analyses at the Korea Basic Science Institute (Daegu, South Korea). Cu K_α radiation (1.54 Å) was employed for this purpose. The actual thicknesses of the nanoparticle arrays were determined from their FE-SEM images, whereas the nominal thicknesses of the different planar layers coated on Si wafers were measured using a surface profiler (KLA-Tencor, P-11). The ten-point maximum peak-to-valley heights and surface areas of the IAOI-NPA and planar ITO film-type electrodes were evaluated by atomic force microscopy (AFM, Park System: XE-100), performed in the tapping mode, at Changwon National University. The sheet resistances of the IAOI-NPA and IAI-NPA electrodes, as well as that of the 90-nm-thick planar ITO film, were measured at three different areas (dimensions of 2.5 × 2.5 cm^2) using a four-point probe system (Mitsubishi Chemical Co., MCP-T600), and averaged subsequently. The specular and total transmittance spectra, as well as the specular and total reflection spectra, of the electrodes were measured covering a wavelength range of 320−800 nm using ultraviolet-visible (UV) spectrophotometry (Varian, Cary 5000). The refractive indices and extinction coefficients of the Ag and AgO_x layers were determined for 20-nm-thick layers by spectroscopic ellipsometry (Ellipso Technology, ElliSEU-am12), performed using the Lorentz oscillator dispersion model, at Ellipso Technology Co., Ltd. (Suwon, South Korea). The mechanical flexibility of the IAOI-NPA and planar ITO film-type electrodes was determined quantitatively using an irreversible two-point bending technique. Electrodes deposited on the PET substrates with dimensions of 2.5 × 2.5 cm^2 were used as specimens for the bending tests. The changes in the electrical resistances of the electrodes were measured as a function of the bending radii of the PET substrates, which were bent using a custom-built two-point bending system. The system consisted of two contact points: one was fixed and the other could move laterally to apply compressive stresses induced by the bending of the PET substrates. The bending test was also performed to determine the variations in the performance parameters of the OSCs under compressive stress induced by mechanical bending of the PET substrates. Five samples were examined and their values averaged for each electrode type.

OSC fabrication and characterization. The two photoactive polymers used for the fabrication of the OSCs, poly[4,8-bis-alkyloxy-benzo[1,2-*b*:4,5-*b*′]dithiophene-2,6-diyl-alt-4-(alkyl-1-one)thieno[3,4-b]thiophene-2,6-diyl] (PBDTTT-C):[6,6]-phenyl-C_{61}-butyric acid ester ($PC_{61}BM$) and PTB7:$PC_{71}BM$, were prepared separately. The electron-donor materials, PBDTTT-C and PTB7, were purchased from 1-Material Chemscitech. The electron-acceptor materials, $PC_{61}BM$ and $PC_{71}BM$, were purchased from Nano-C and were used as received. First, a PEDOT:PSS layer with a thickness of approximately 50 nm was deposited on the IAOI-NPA and on planar ITO film-based electrodes because further increases in the thickness of the PEDOT:PSS layer led to significant reductions in the external quantum efficiency and increases in the dark current density. A solution of PEDOT-PSS (Clevios P, VP AI 4083) in isopropyl alcohol (IPA) at a ratio of PEDOT-PSS:IPA = 1:2 vol% was spin-coated on the electrodes at 5000 rpm for 40 s in a glove box. Layers of the photoactive polymers with a thickness of approximately 100 nm were subsequently deposited on the PEDOT-PSS layer. The thickness of the photoactive polymer was chosen at the relatively small value to avoid abrupt reductions in the photovoltaic performances. A low charge carrier mobility and short exciton diffusion length in the photoactive polymer requires this thickness to remain as low as possible, to improve charge extraction efficiency by suppressing charge recombination. A solution of PBDTTT-C:$PC_{61}BM$ was formed by dissolving the mixture (10 mg:20 mg) in dichlorobenzene (1 ml), whereas a solution of PTB-7:$PC_{71}BM$ was prepared by dissolving the mixture (8 mg:12 mg) in chlorobenzene (1 ml). After the solutions had been stirred at 50 °C for 12 h, a volume fraction of 3% of 1,8-diiodooctane (Sigma Aldrich) was added to the solutions. The stirred solutions were then passed through a 0.2-μm poly(tetrafluoroethylene) syringe filter, and layers of the photoactive polymers were deposited onto the poly(3,4-ethylenedioxythiophene):poly(styrenesulfonate) (PEDOT:PSS) layer by spin coating at 800 rpm for 40 s. The multilayers of PEDOT:PSS/PBDTTT-C:$PC_{61}BM$ and PEDOT:PSS/PTB7:$PC_{71}BM$, deposited on the electrodes, were then baked in a glove box at a relatively low temperature (100 °C) for 5 min to prevent the PET substrates from deforming. Finally, an Al layer was deposited as top metal cathode by thermal evaporation in a vacuum of approximately 6.6 × 10^{-7} Pa. The active device area (A) of approximately 0.38 cm^2 was defined using a shadow mask during the Al-evaporation process. The device area is comparable or even larger than the areas in the range of 0.04–0.138 cm^2 that have been frequently reported in the literature.[14,28–31]

The performances of the OSCs were determined using an air mass 1.5 global (AM 1.5G) solar simulator (Oriel 300 W) with a light intensity of 100 mW cm^{-2}. The photovoltaic performance parameters were averaged with standard deviations for 10 specimens. There were no noticeable differences in these values between OSC specimens that were prepared by separate device fabrication runs. The solar simulator was standardized using a standard photovoltaic (PV) reference cell (5 cm × 5 cm area), based on monocrystalline silicon, which was calibrated at the National Renewable Energy Laboratory (NREL) (Colorado, USA). The *J*–*V* characteristics were measured with a Keithley 2400 source meter. The series (R_s) and shunt (R_{sh}) resistances were determined from the slopes of the dark *J*–*V* characteristic curve that was fitted with the following Shockley diode equation:[32]

$$J = J_0\left\{\exp\left[\frac{q(V - AJR_s)}{nkT}\right] - 1\right\} + \frac{V - AJR_s}{AR_{sh}} - J_{ph} \quad (1)$$

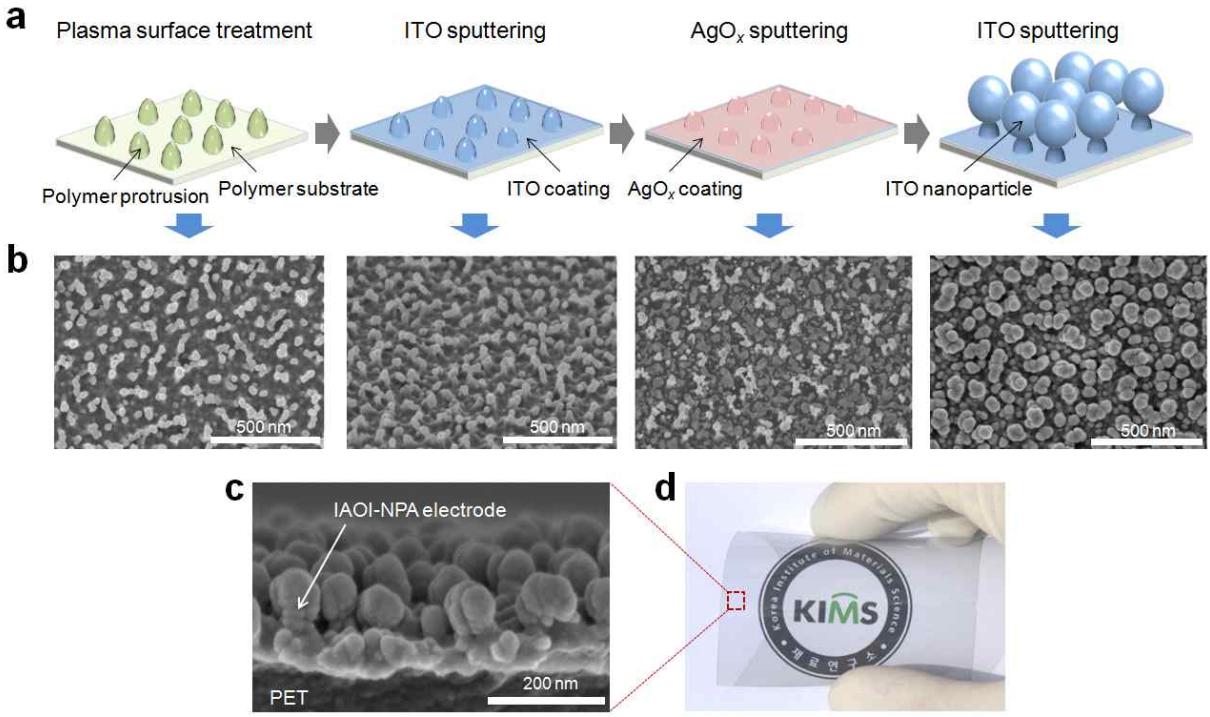

Fig. 1 (a) Schematic diagrams representing the fabrication procedure of the proposed IAOI-NPA electrode on a PET substrate. (b) FE-SEM images illustrating the morphological evolution of the IAOI-NPA electrode on the polymer protrusions. (c) A cross-sectional FE-SEM image of the IAOI-NPA electrode. (d) A photograph of a highly flexible PET substrate coated with the IAOI-NPA electrode.

where J is the current density, J_{ph} is the voltage-dependent photogenerated current density, J_0 is the reverse saturation current density, q is the elementary charge, n is the diode ideality factor, k is the Boltzmann constant, and T is the absolute temperature. The fill factor (FF), defined as the ratio of the maximum power delivered by the product of the open circuit voltage (V_{oc}) and the short circuit current density (J_{sc}), was measured from the maximum squareness of the J–V characteristic curve.[33] The PCE was determined from the following equation:

$$\mathrm{PCE} = \frac{J_{sc} V_{oc} \mathrm{FF}}{P_{in}} \qquad (2)$$

where P_{in} is the incident light power that was 100 mW cm^{-2} in this study. The incident photon-to-current efficiency (IPCE) spectra (Oriel IQE-200) were determined using a quantum-efficiency measurement system consisting of a 250-W quartz tungsten halogen lamp as light source, a monochromator, an optical chopper, a lock-in amplifier, and a calibrated silicon photodetector. The OSCs were equipped with a 0.38-cm^2 metal aperture during the performance measurements to avoid any performance overestimation.

Results and discussion

The 3D IAOI-NPA electrode was synthesized on a PET substrate by the following sequence of processes: (*i*) the plasma-induced pre-treatment of the PET surface and (*ii*) the successive depositions of ITO, AgO$_x$, and ITO through magnetron sputtering (Fig. 1a and b). The fabricated NPA exhibited a unique morphology in that it consisted of a quasi-periodic pattern of discrete, globular ITO nanoparticles, which were superimposed on a continuous ITO–AgO$_x$–ITO multilayer (Fig. 1c). During the PET pre-treatment process, densely packed nanoscopic polymer protrusions evolved on the surface of the PET substrate as a result of the plasma-induced ion irradiation. Such nanoscopic polymer protrusions under the influence of plasmas were frequently observed in numerous investigations. Researchers speculated that these protrusions develop on polymer surfaces via various surface dynamic phenomena—including surface migration, etching, redeposition, and agglomeration—of highly volatile low-molecular-weight (LMW) polymer chains that form at the top surface of polymer substrates by random ion-induced chain scission.[34–41] In this study, the nanoscopic polymer protrusions developed with a morphological feature in form of elongated globular shapes (Fig. S1). It was further observed that an increase in the pre-treatment time led to an increase in the dimension of the polymer protrusions and an increase in the distance between neighbouring protrusions, owing to coalescence of the protrusions with their neighbours. The average values of the height of polymer protrusions and the distance between them were approximately 70 nm and 110 nm, respectively, at a 3-min pre-treatment time applied in the present study.

Interestingly, the complex hybrid structure of the 3D IAOI-NPA electrode self-assembled spontaneously on the polymer surface during the sequential sputtering processes. The growth of the 3D electrode on these polymer protrusions was self-

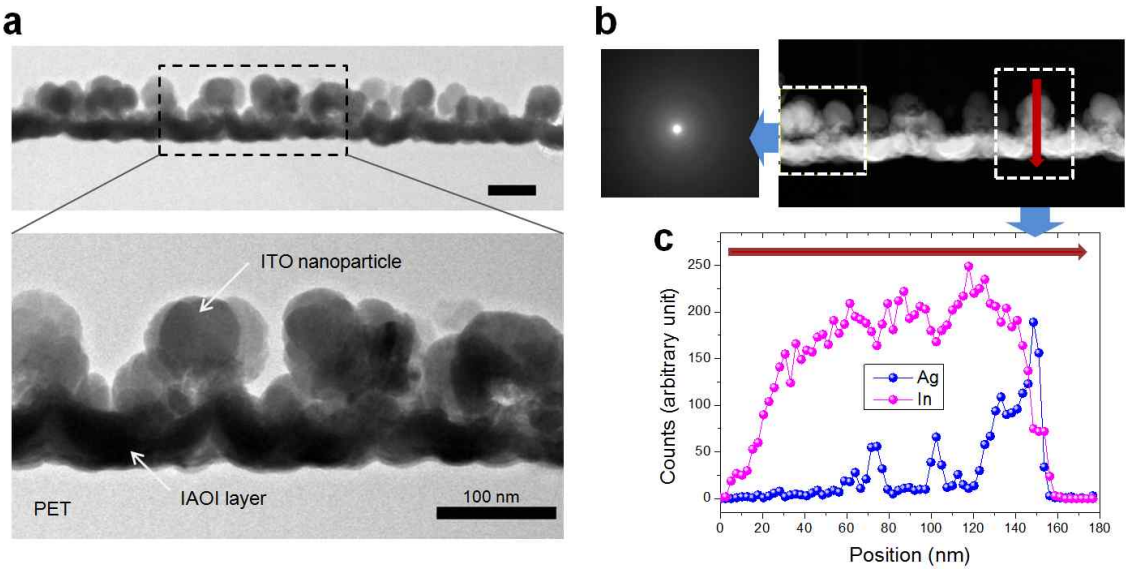

Fig. 2 Composition and structure of an IAOI-NPA electrode on a PET substrate. (a) Bright-field and magnified part of a TEM image of the IAOI-NPA electrode, coated on a PET surface, which was treated with an Ar plasma for 3 min. (b) A STEM image and SAED pattern illustrating the amorphous nature of the IAOI-NPA electrode. (c) EDS spectra of the elements Ag and In demonstrating the chemical compositions of different areas of the electrode corresponding to (b).

sustained and clearly different from the growth mode of planar TCO films. It was found that the existence of the polymer protrusions facilitated the preferential growth of oxide nanoparticles on the topmost surfaces of the protrusions during the subsequent vacuum sputtering of oxide phases, consisting of the sequential sputtering of ITO, AgO_x, and ITO layers. During the early sputtering stages of the oxide layers, the oxides were deposited over most of the PET surface including both the polymer protrusions and the recessed surfaces between them. However, further oxide deposition was stimulated predominantly on the top surfaces of the polymer protrusions, probably owing to relatively large fluxes of oxide-reactive species. On the other hand, the oxide deposition on the recessed surfaces was seriously restrained by the shortage of oxide-reactive species caused by a shadowing effect by the growing oxide nanoparticles on the polymer protrusions. It was readily expected that the strong cohesion between oxide molecules, compared to the adhesion between oxide and PET, restrained the contact of the oxide nanoparticles on the top surface of the polymer protrusions, while the nanoparticles formed a globular morphology to reduce the surface energy.[41–43] As a result of the preferential development of oxide nanoparticles on the polymer protrusions, the number density of oxide nanoparticles, which is directly proportional to the number of polymer protrusions, was also reduced by the increase of the pre-treatment time. Here, the preferential growth of the NPA on the polymer protrusions with a quasi-periodic pattern allowed the dimensions and distribution of the nanoparticles to be controlled within a sub-wavelength range, thereby inducing strong antireflective characteristics and, thus, a high transmission could be achieved (Fig. 1c and d). It was readily noticed that the 3D IAOI-NPA electrode exhibited a high optical transmittance, especially in view of the fact that a semitransparent AgO_x layer was embedded within it. It has been reported that the insertion of a thin Ag layer between transparent oxide films in a conventional oxide–metal–oxide (OMO) configuration results in a relatively poor average transmittance of about 80% in the visible spectral range, although a maximum transmittance of about 90% was reached over a narrow spectral window. This can be attributed to the high reflectivity of the Ag layer, especially at longer wavelengths of the incident light.[44] The nature of this AgO_x layer and its effects on the optical and electrical properties of the IAOI-NPA electrode will be discussed in detail later.

The structural and chemical characteristics of the IAOI-NPA electrode were evaluated using cross-sectional STEM, EDS, and selective-area electron diffraction (SAED) analyses. The IAOI-NPA electrode was fabricated by (*i*) forming polymer protrusions on the PET polymer substrate by subjecting it to a 3-min Ar plasma-induced pretreatment and (*ii*)

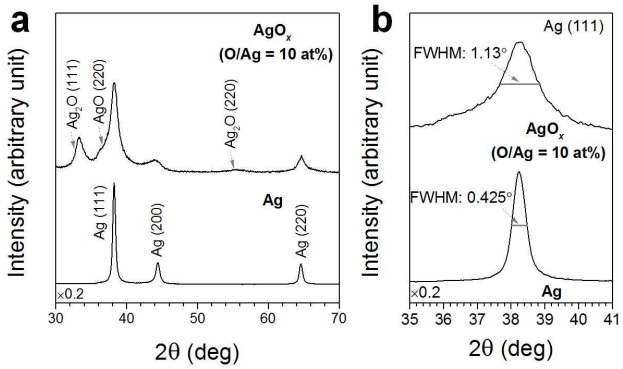

Fig. 3 (a) Crystalline structures and (b) FWHM values of the Ag (111) peak in pure Ag and AgO_x (O/Ag = 10 at%) layers, determined by GI-XRD measurements.

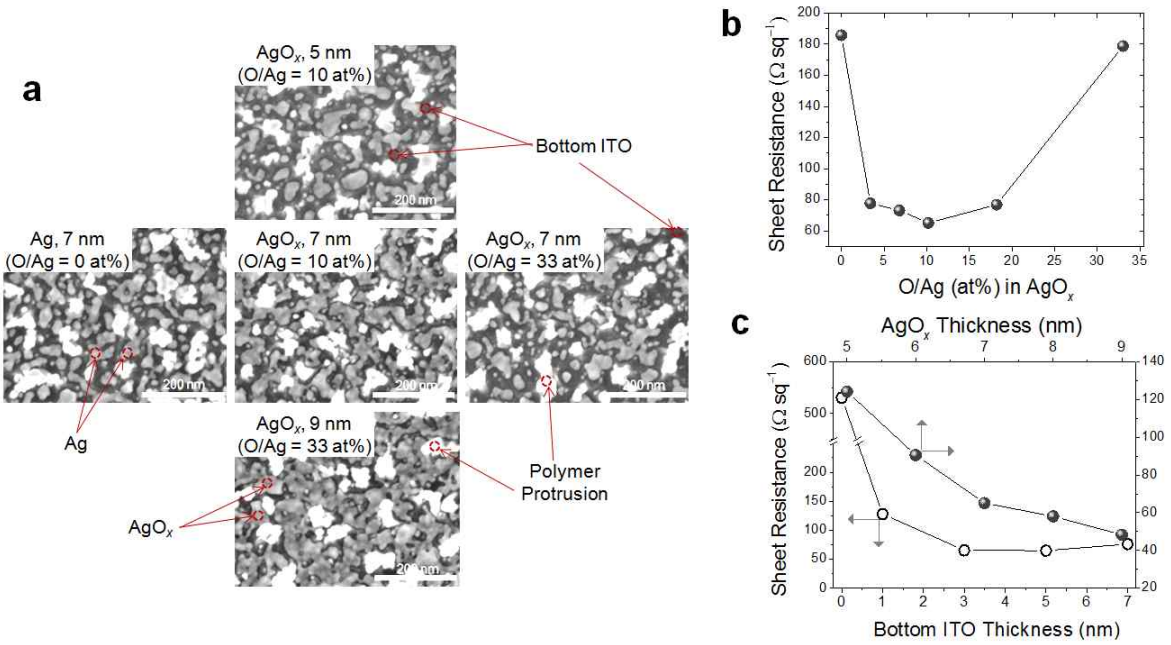

Fig. 4 (a) FE-SEM images showing the morphological differences between 7-nm-thick AgO_x layers deposited on 5-nm-thick ITO layers with the following O/Ag ratios: 0, 10, and 33% and (*ii*) AgO_x (O/Ag = 10 at%) layers deposited on 5-nm-thick ITO layers with the following thicknesses: 5, 7, and 9 nm. The pre-treatment time for the PET surface was set at 3 min. Changes in sheet resistance of the IAOI-NPA electrodes for (b) different O/Ag ratios of the 7-nm-thick AgO_x layers and (c) different thicknesses of the AgO_x (O/Ag = 10 at%) and the bottom ITO layer for a 7-nm-thick AgO_x (O/Ag = 10 at%) layer.

subsequent deposition of ITO, AgO_x (O/Ag = 10 at%), and ITO coatings on the pre-treated PET surface; the nominal thicknesses of these coatings were 5 nm, 7 nm, and 60 nm, respectively. We verified that the fabricated IAOI-NPA electrode was composed of discrete globular nanoparticles with an average size of approximately 100 nm, superimposed on a continuous multilayer with a thickness of approximately 50 nm (Fig. 2a). The SAED pattern of the IAOI-NPA electrode suggested that ITO was amorphous (Fig. 2b). The chemical composition of the electrode was investigated in depth using EDS (Fig. 2c). Elemental Ag was detected only in the bottom domain of the continuous multilayer, while elemental In was detected in all continuous layers and nanoparticles. The results proved that the IAOI-NPA electrode consisted of globular ITO nanoparticles and a subjacent IAOI multilayer, in which the sandwiched ultrathin AgO_x layer provided the primary electrical path.

The oxidation caused noticeable changes in the crystallographic properties of the Ag layer. The crystallographic properties of the AgO_x (O/Ag = 10 at%) layer were determined by GI-XRD analyses and were compared with those of a pure Ag layer (Fig. 3). The peaks attributable to pure Ag, namely the peak for Ag (111) at 38.2°, that for Ag (200) at 44.4°, and that for Ag (220) at 64.6°, were of significantly lower intensities in case of the AgO_x (O/Ag = 10 at%) layer (Fig. 3a). The broadening of the Ag (111) peak, represented by its full width at half maximum (FWHM), occurred by Ag oxidation and covered an angular range from 0.425° to 1.13° owing to the transition of pure Ag to AgO_x (O/Ag = 10 at%) (Fig. 3b). This indicates a build-up of microstrains in the Ag lattice and a reduction of the crystallite size, because of oxidization. The crystallite size, calculated by the Scherrer equation using the FWHM of the Ag (111) peak, reduced from 17.9 nm to 7.6 nm as the O/Ag ratio increased from pure Ag to 10 at%. Such a reduction of the Ag crystallite size in the AgO_x (O/Ag = 10 at%) layer might be directly associated with the evolution of AgO_x crystallites originating from an increased density of AgO_x nuclei during the early nucleation stages. The intensive growth competition between densely distributed AgO_x nuclei restrained the increase in crystallite size. When the crystalline phases and orientations were determined by comparing the peak positions with the reported data in the literature,[45,46] the appearance of a much broader peak at approximately 33.4° indicated the development of a mixed phase of AgO and Ag_2O with poor crystallinity and small dimensions in the AgO_x (O/Ag = 10 at%) layer. When the oxidation state of the AgO_x (O/Ag = 10 at%) layer was further investigated by XPS (Fig. S2), negative shift of the binding energy of the Ag 3d peaks, accepted as criterion for Ag oxidation,[47–51] was inappreciable as the O/Ag ratio increased to 10 at%. Furthermore, the deconvolution of the Ag $3d_{3/5}$ peak indicated the inclusion of a small amount (2.7%) of the Ag_2O crystalline phase (367.6 eV) in the AgO_x (O/Ag = 10 at%) layer, whereas the percentage of this Ag_2O phase strongly increased in case of a highly oxidized AgO_x (O/Ag = 33 at%) layer.

The thin AgO_x (O/Ag = 10 at%) layer, which was deposited between the ITO films in the IAOI multilayer, played a vital role in reducing the electrical resistance of the overall IAOI-

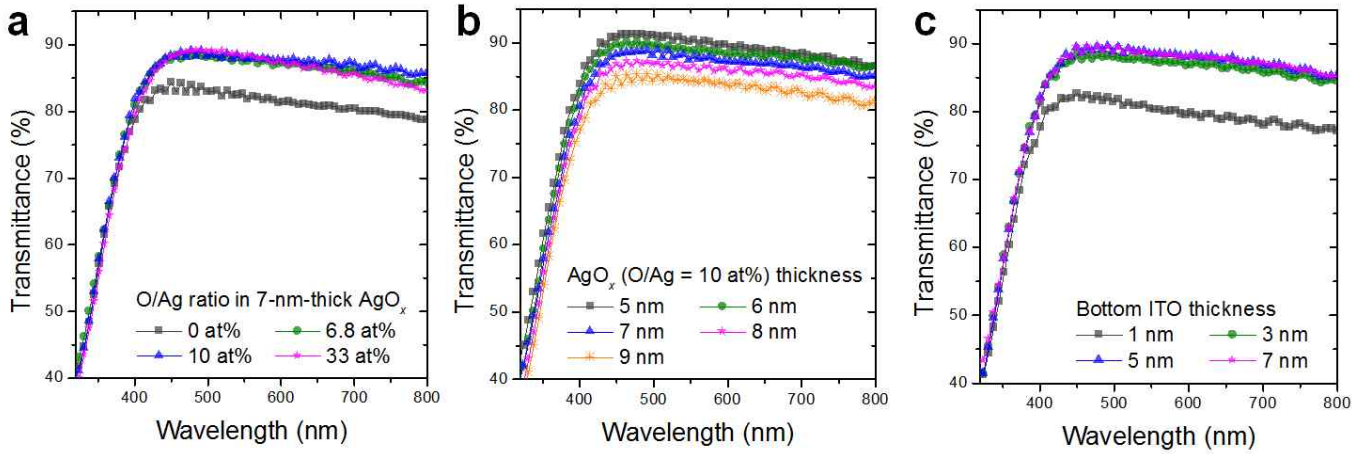

Fig. 5 Changes in the specular transmittances of the IAOI-NPA electrodes with changes in (a) the O/Ag atomic ratio in 7-nm-thick AgO_x layers, (b) the thickness of the AgO_x (O/Ag = 10 at%) layer, and (c) the thickness of the bottom ITO layer located below the 7-nm-thick AgO_x (O/Ag = 10 at%) layer. The pre-treatment time for the PET surface was set at 3 min.

NPA electrode by outperforming pure Ag layers as the major conductive route. Although the discrete ITO nanoparticles in the NPA played a predominant role in the extraction of charges from the photoactive polymers because of their 3D geometry, the nanoparticles did not contribute substantially to the reduction of the electrical resistance of the IAOI-NPA electrode. Compared to the 3D electrode that did not contain an embedded Ag or AgO_x layer and that exhibited a sheet resistance of more than 250 Ω sq^{-1}, the IAOI-NPA electrode showed a much lower sheet resistance, thereby confirming the improvement in its charge collection owing to the formation of highly conductive paths in the sandwiched metallic layer. The difference between pure Ag and AgO_x (O/Ag = 10 at%) layers is caused by differences in their wettabilities between the ITO films. It was impossible to form continuous metallic layers that completely cover the bottom ITO films, regardless of the thickness of the metallic layers, because of the existence of polymer protrusions. Instead, the deposition conditions of the embedded metallic layers were set to reduce the percolation-threshold thickness that corresponds to the minimum possible thickness that is still providing sufficient electrical paths. The thickness should be minimized because the optical transmission of the overall IAOI-NPA electrode degraded significantly on increasing thickness of the metallic layers.

UHR FE-SEM measurements demonstrated that the wettabilities of the metallic layers were strongly affected by different oxygen-inclusion levels and different layer thicknesses (Fig. 4a). Although the Ag and AgO_x layers both covered the bottom ITO layer only incompletely at a thickness of 7 nm, FE-SEM images indicated that the AgO_x (O/Ag = 10 at%) layer exhibited a higher wettability on the bottom ITO layer than the pure Ag and highly oxidized Ag layer with O/Ag = 33 at% (Fig. 4a). The wettability of the AgO_x (O/Ag = 10 at%) layer improved further on increasing thickness. As a result, the minimum sheet resistance of the IAOI-NPA electrode employing a 7-nm-thick metallic layer was found at O/Ag = 10 at%, when the AgO_x layer was deposited on 5-nm-thick ITO bottom layers that, in turn, were deposited on PET surfaces pre-treated for 3 min (Fig. 4b). In contrast, the electrode employing a pure Ag layer of the same thickness exhibited a significantly higher sheet resistance owing to its much poorer wettability on the bottom ITO layer. It was also found that the bottom ITO layer on the PET substrate should have a thickness of more than 3 nm (Fig. 4c). The ITO layer seemed to provide a surface with a higher free energy for the AgO_x coating in comparison to the polymer surfaces which were relatively inert. The sheet resistance of the electrode was further reduced to less than 50 Ω sq^{-1} at a thickness increase of the AgO_x (O/Ag = 10 at%) layer to 9 nm, accompanied by a substantially improved wettability of the AgO_x layer on the bottom ITO layer (Fig. 4c).

The optical transmission of the IAOI-NPA electrode was affected by variations in the oxidation level and thickness of the embedded AgO_x layer, as well as by the thickness of the bottom ITO film (Fig. 5). The specular transmittance of the electrode was optimized in case the AgO_x layer had an O/Ag ratio of at least 6.8 at% (Fig. 5a). The IAOI-NPA electrode with a 7-nm-thick AgO_x (O/Ag = 10 at%) layer exhibited a specular transmittance of 89% at a wavelength of approximately 500 nm, whereas the electrode with a 7-nm-thick pure Ag layer exhibited a lower transmittance (83%) at the same wavelength. The superior optical transmittances of the electrodes employing AgO_x layers rather than a pure Ag layer can be attributed to (*i*) the reduction in the reflection of light at the interfaces between the AgO_x and ITO layers and (*ii*) the reduction in the absorbance of light at the AgO_x layer compared to the Ag layer. The AgO_x (O/Ag = 10 at%) layer exhibited a refractive index of about 0.5 in the visible spectral range, whereas that of Ag layer was about 0.2 (Fig. S3a). The higher refractive indices of the AgO_x layers led to a decrease in the amount of incident light reflected at the interface between the AgO_x (O/Ag = 10 at%) and the ITO layers. This happens because of the improved matching of the optical impedances of the AgO_x and ITO layers, which have refractive indices of 1.78–2.12 in the IAOI configuration.[52] A comparison of the specular reflections of the

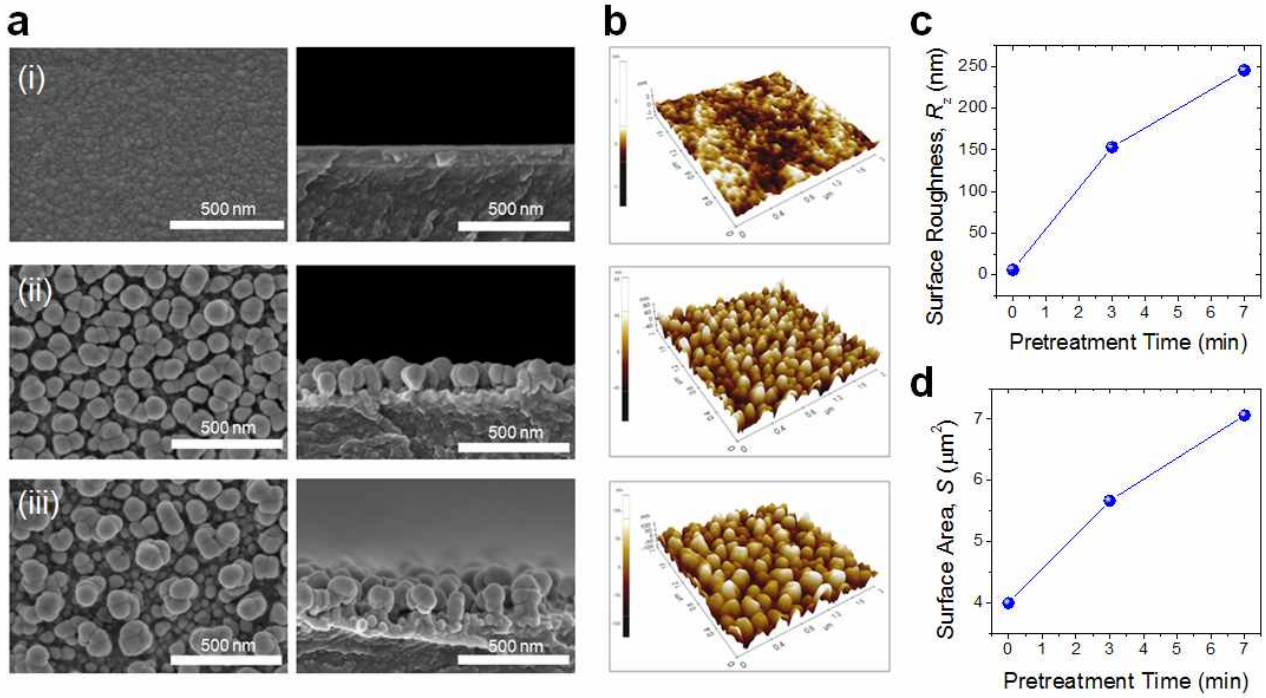

Fig. 6 (a) Cross-sectional FE-SEM images and (b) 3-D AFM images showing the morphologies of (*i*) a planar IAOI film-type electrode fabricated on an untreated PET surface, (*ii*) a 3D IAOI-NPA electrode fabricated on a PET surface pre-treated for 3 min, and (*iii*) a 3D IAOI-NPA electrode fabricated on a PET surface pre-treated for 7 min. (c) Surface roughnesses and (d) surface areas of the IAOI-NPA electrodes as a function of the pre-treatment time of the PET surface.

IAOI-NPA electrodes employing AgO_x and Ag layers confirmed the superior antireflective characteristics of the AgO_x (O/Ag = 10 at%) layer in the electrode (Fig. S4). Furthermore, concerning the AgO_x layer, the significantly lower extinction coefficients of 0.6–2.5 in the visible spectral range successfully reduced the absorbance of incident light passing through the layer, in contrast to the pure Ag layer with relatively high extinction coefficients of 0.6–5.2 in the visible range (Fig. S3b). The transmittance of the electrode employing the Ag layer might be further reduced by non-negligible absorption and scattering of incident light caused by the more highly discontinuous and granular morphology of the Ag layer in comparison to the AgO_x layer. By balancing the electrical conductivity (Fig. 4) against the optical transmission (Fig. 5), the sheet resistance and specular transmittance of the electrode could be optimized at 65 Ω sq^{-1} and 89% at a wavelength of 500 nm, respectively. This involved the use of a 7-nm-thick AgO_x (O/Ag = 10 at%) layer, sandwiched between 5-nm-thick ITO bottom and 60-nm-thick ITO top layers. In fact, although the use of a 9-nm-thick AgO_x (O/Ag = 10 at%) layer resulted in a sheet resistance of less than 50 Ω sq^{-1}, the thicker AgO_x layer caused a significantly poorer specular transmittance of 85%.

Discrete ITO nanoparticles developed on the IAOI multilayer with different dimensions and number densities, exerting immediate influence on the charge transport and separation efficiency, by applying different pre-treatment times for the PET substrates. The morphological evolution of the ITO nanoparticles in the IAOI-NPA electrode was determined by FE-SEM and AFM measurements (Fig. 6). Since the interparticle distance and size of the polymer protrusions increased linearly on increasing pre-treatment time, owing to the continuous coalescence of neighbouring protrusions, the preferential growth of ITO nanoparticles on the topmost surfaces of the polymer protrusions led to the formation of fewer and larger ITO nanoparticles with an increase in the pre-treatment time (Fig. 6a and b). When the pre-treatment time was increased from 3 min to 7 min, the distance between the ITO nanoparticles increased from 110 nm to 190 nm. This evolution of the nanoparticles was accompanied by a significant increase in the surface roughness and surface area of the 3D electrode (Fig. 6c and d). The ten-point maximum peak-to-valley height roughness (R_z) of the electrode, which was proportional to the height of the ITO nanoparticles, increased from 6 nm to 153 nm as the pre-treatment time increased from 0 min to 3 min. The R_z value reached 245 nm for a pre-treatment time of 7 min. This increase of the R_z value on increasing pre-treatment time was accompanied by an increase in the total area of the curved surface (S) of the electrode (Fig. 6d). When compared to a 90-nm-thick planar ITO film-type electrode, fabricated on a pristine PET substrate without ITO nanoparticles, the 3D IAOI-NPA electrode fabricated on a PET substrate that was pre-treated for 3 min (labelled IAOI-NPA (3 min)) exhibited a surface area that was greater by 42%. Similarly, the IAOI-NPA electrode fabricated on a PET substrate that was pre-treated for 7 min (labelled IAOI-NPA (7 min)) had a surface area that was larger by 77%. It was readily

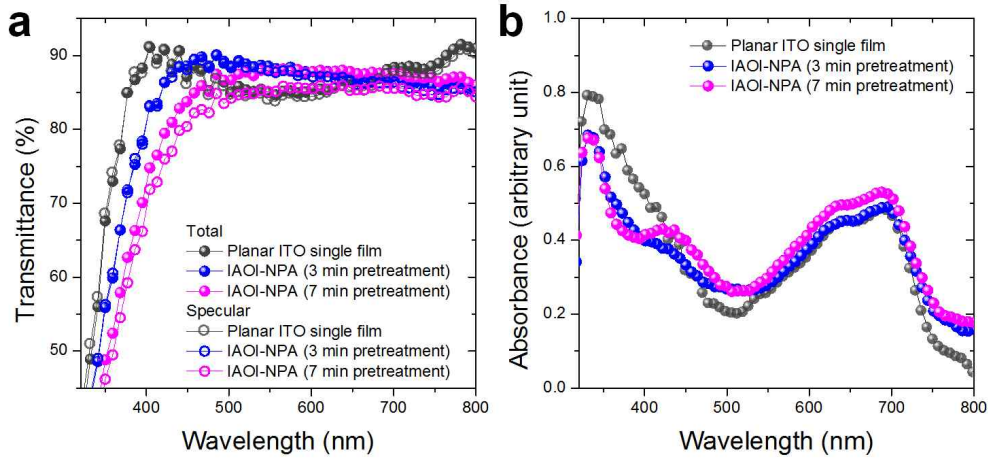

Fig. 7 (a) Total and specular transmittances of a 90-nm-thick ITO planar film-based electrode fabricated on an untreated PET surface, and of 3D IAOI-NPA electrodes fabricated on PET surfaces pretreated for 3 and 7 min. (b) Absorbance of incident light in a buffer polymer layer of PEDOT:PSS and a photoactive polymer layer of PBDTTT-C:$PC_{61}BM$, coated on the electrodes corresponding to (a).

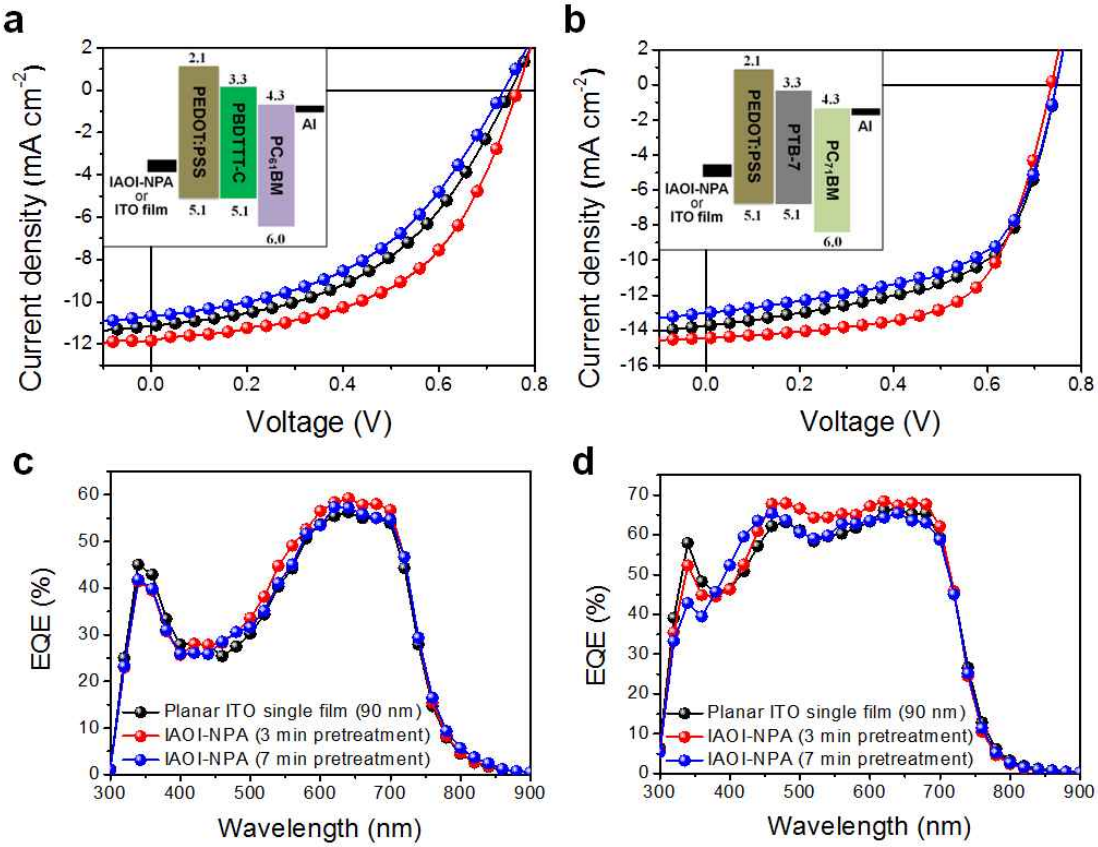

Fig. 8 Current density versus voltage (J–V) characteristics under AM 1.5 G illumination (100 mW cm^{-2}) of OSCs with the following photoactive polymers: (a) PBDTTT-C:$PC_{61}BM$ and (b) PTB-7:$PC_{71}BM$; these layers were deposited on a 90-nm-thick planar ITO film-based electrode on a pristine PET substrate, the IAOI-NPA electrode on the PET substrate that was pre-treated for 3 min, and the IAOI-NPA electrode on the 7-min-pre-treated PET substrate. The insets show schematic energy diagrams of the electronic structures of the OSCs. EQE spectra of the OSCs with the following polymers as photoactive layer: (c) PBDTTT-C:$PC_{61}BM$ and (d) PTB-7:$PC_{71}BM$.

expected that the ITO nanoparticles in the IAOI-NPA electrode acted as directly conducting pathways for charge-carrier transport, and the increase of their surface area led to improvements in the collection of charged carriers within the photoactive polymers.

The 3D geometry of the IAOI-NPA electrodes, predominantly caused by ITO nanoparticles, did not generate noticeable absorbance and scattering of the incident light. In the visible spectral range, the IAOI-NPA electrodes exhibited total transmittances that were comparable to that of a 90-nm-thick

Table 1 Photovoltaic performance parameters of OSCs, averaged for 10 specimens that were determined under simulated AM 1.5G illumination with an irradiance of 100 mW cm^{-2}.

Photoactive Polymers	Electrode	J_{sc} [mA cm^{-2}]	V_{oc} [V]	FF [%]	R_{sh} [Ω cm^2]	R_s [Ω cm^2]	PCE [%]
PBDTTT-C: $PC_{61}BM$	Planar ITO film	11.12 ± 0.39	0.74 ± 0.01	45.84 ± 1.26	1.2×10^4	8.23	3.80 ± 0.07
	IAOI-NPA (3 min)	11.72 ± 0.13	0.76 ± 0.01	51.91 ± 0.01	2.3×10^4	6.21	4.64 ± 0.10
	IAOI-NPA (7 min)	10.91 ± 0.29	0.74 ± 0.01	43.83 ± 0.02	8.9×10^3	9.65	3.54 ± 0.15
PTB-7: $PC_{71}BM$	Planar ITO film	13.73 ± 0.10	0.74 ± 0.01	59.01 ± 0.61	6.2×10^4	4.35	6.05 ± 0.06
	IAOI-NPA (3 min)	14.58 ± 0.17	0.74 ± 0.01	62.41 ± 0.81	7.2×10^4	3.11	6.74 ± 0.05
	IAOI-NPA (7 min)	13.07 ± 0.66	0.74 ± 0.01	57.67 ± 0.83	5.7×10^4	5.06	5.63 ± 0.35

ITO film-based electrode (Fig. 7a). This optical property can be attributed to the suppression of light reflection through control of the interparticle distance and size of the ITO nanoparticles within a sub-wavelength range. There was no difference between the total and specular transmittances of the IAOI-NPA (3 min) electrode, indicating that the scattering of incident light was not significant. On the other hand, there was a small difference between the total and specular transmittances of the IAOI-NPA (7 min) electrode as a result of an increase in light scattering which, in turn, led to an increase in the length of diffusion paths of the photons in the photoactive layer. The increase in light scattering can be ascribed to interference of the incident light in the IAOI-NPA (7 min) electrode, in which the interparticle distance and the nanoparticle size both were in the range of approximately 200 nm. The absorbance of incident light in the photoactive polymer layer, which consisted of a bulk heterojunction of PBDTTT-C as electron donor and $PC_{61}BM$ as electron acceptor, was determined for the IAOI-NPA and planar ITO film-based electrodes. It was found that there was no significant difference in the absorbances of the PBDTTT-C:$PC_{61}BM$ layers coated on the different electrodes (Fig. 7b).

The current density–voltage (*J–V*) characteristics and external quantum efficiency (EQE) spectra of OSCs, based on the planar ITO and IAOI-NPA (3 and 7 min) electrodes, are compared in Fig. 8. Two different bulk heterojunction configurations, employing photoactive polymers with low bandgaps, thereby providing high power-conversion efficiencies because they can absorb incident light of relatively longer wavelengths (up to 750 nm), were used in order to illustrate the relative merits of using the 3D IAOI-NPA electrode instead of the planar ITO electrode in OSCs. The photoactive layers were mixed bulk heterojunctions comprising (*i*) PBDTTT-C as electron donor and $PC_{61}BM$ as electron acceptor and (*ii*) PTB-7 as electron donor and $PC_{71}BM$ as electron acceptor. PEDOT:PSS was used as hole-injection material because its work function matches well with those of the aforementioned electron donor materials (see insets in Fig. 8a and b). The *J–V* characteristics and EQE spectra of OSCs based on the PBDTTT-C:$PC_{61}BM$ (Fig. 8a and c) and PTB-7:$PC_{71}BM$ (Fig. 8b and d) bulk heterojunctions were determined under both AM 1.5G illumination and dark condition. The device performances of the OSCs—including their short-circuit current density (J_{sc}), open-circuit voltage (V_{oc}), fill factor (FF), device series resistance (R_s), shunt resistance (R_{sh}), and PCE—were determined from their *J–V* characteristics (Table 1). When the J_{sc} was compared with the integrated J_{sc}, which was determined from IPCE spectra (Table S1), the differences of less than 5% indicated that the measurements were quite accurate without serious overestimation for the device performances. The In the case of PBDTTT-C:$PC_{61}BM$ heterojunctions, the OSC based on the IAOI-NPA (3 min) electrode exhibited the highest average PCE of 4.64 ± 0.10%, whereas the OSCs with the IAOI-NPA (7 min) and planar ITO film-based electrodes exhibited average PCEs of 3.54 ± 0.15% and 3.80 ± 0.07%, respectively. It is obvious that the PCE improvement in case of the OSC that is based on the IAOI-NPA (3 min) electrode was not caused by the differences in the optical transmittances of the examined electrodes, as discussed above. This conclusion is supported by the EQE spectra of the OSCs. There was no significant difference in the EQE spectra of OSCs based on different electrodes, but for the same photoactive polymer. All electrodes resulted in similar EQE values at wavelengths in the range of 300−900 nm: 30–60% for PBDTTT-C:$PC_{61}BM$ and 50–69% for PTB-7:$PC_{71}BM$ (Fig. 8c and d).

It might be reasonable to ascribe the increase in the PCE to the fact that the charge transport and separation across the IAOI-NPA (3 min) electrode were favourably enhanced owing to both, the increased surface area and reduced effective series resistance for hole transport. In addition, the leakage current in the electrode was negligible. The surface area of the IAOI-NPA (3 min) electrode was compared with that of the 90-nm-thick planar ITO film-based electrode. The surface area of the former was higher by 42% owing to the nanoparticles. Furthermore, the R_s value of the IAOI-NPA (3 min) electrode (determined from the *J–V* curve of the OSC at 1.0 V under dark illumination) was lower by 25%, whereas its R_{sh} value (determined from the *J–V* curve at 0 V under dark illumination) was higher by 48%. It is known that a higher R_{sh} value, indicating a lower leakage current across the cell, results in an improved PCE.[53,54] More evidence for the conclusion that the IAOI-NPA (3 min) electrode was effectively preventing the leakage current was the fact that the corresponding OSC exhibited a high rectification

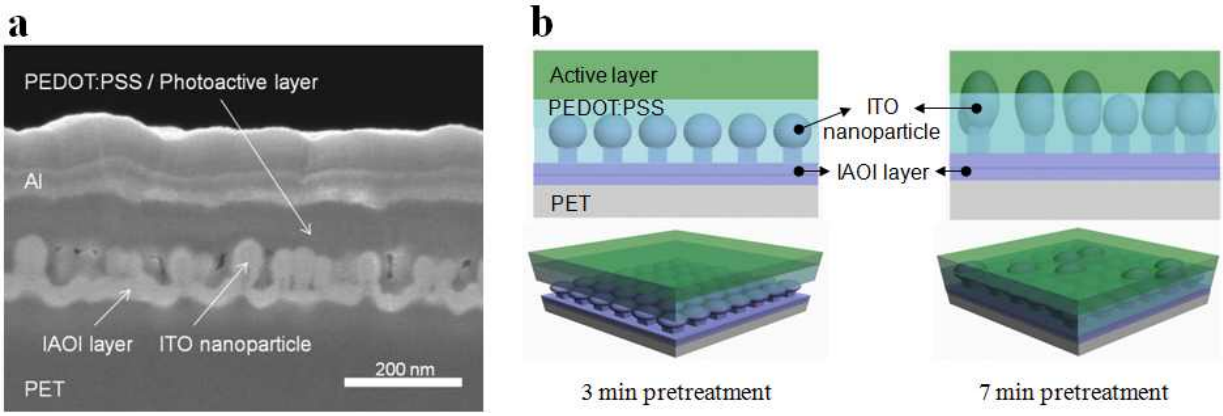

Fig. 9 (a) Cross-sectional view of a flexible OSC with the following device architecture: PET/IAOI-NPA (3 min) anode/PEDOT-PSS/PBDTTT-C–$PC_{61}BM$/Al cathode. (b) Schematic illustration of the possible device geometries of the OSCs fabricated using the IAOI-NPA anode on PET surfaces pretreated for different time periods (3 and 7 min).

ratio (defined as the current ratio at ±1 V of the dark curve) of 6.65×10^3, in contrast to the ratio of the OSC based on the planar ITO film-based electrode (3.26×10^2).

Although the surface area of the IAOI-NPA (7 min) electrode was still higher (77% greater) than that of the planar ITO electrode, the equivalent OSC exhibited a significantly lower PCE value than that of the OSC based on the IAOI-NPA (3 min) electrode. Further, the PCE value of the OSC based on the IAOI-NPA (7 min) electrode was yet lower than that of the OSC based on the planar ITO film-based electrode. It should be noted that detrimental changes in R_s and R_{sh}, which are directly attributable to the generation of a non-negligible leakage current, occurred on increasing the pre-treatment time from 3 to 7 min. A cross-sectional FE-SEM image of the OSC based on the IAOI-NPA (3 min) electrode shows that the polymer multilayer of PEDOT:PSS (50 nm)/PBDTTT-C:$PC_{61}BM$ (100 nm), deposited on the IAOI-NPA (3 min) electrode, had a thickness of well above 100 nm and that no abnormal ITO nanoparticles projected into the polymer multilayer (Fig. 9a). On the basis of this morphology of the electrode, it was expected that the ITO nanoparticles in the electrode were completely covered by the PEDOT:PSS layer and were not in contact with the photoactive layer (i.e., the PBDTTT-C:$PC_{61}BM$ layer) (Fig. 9b). As a result, a leakage current was successfully prevented from flowing in the OSC, based on the IAOI-NPA (3 min) electrode. However, a similarly desirable configuration and morphology could not be noticed in the case of the polymer multilayer deposited on the IAOI-NPA (7 min) electrode. The ITO nanoparticles in the IAOI-NPA (7 min) electrode, exhibiting further increases in their dimension and interparticle distance (with R_z being 245 nm), as discussed above, could penetrate through the 50-nm-thick PEDOT:PSS layer and were in direct contact with the photoactive layer. This undesirable structural configuration led to the generation of a leakage current, resulting in the degraded performance of the OSC.

The performance characteristics of the OSCs based on the IAOI-NPA electrodes were similar to that of the OSC with

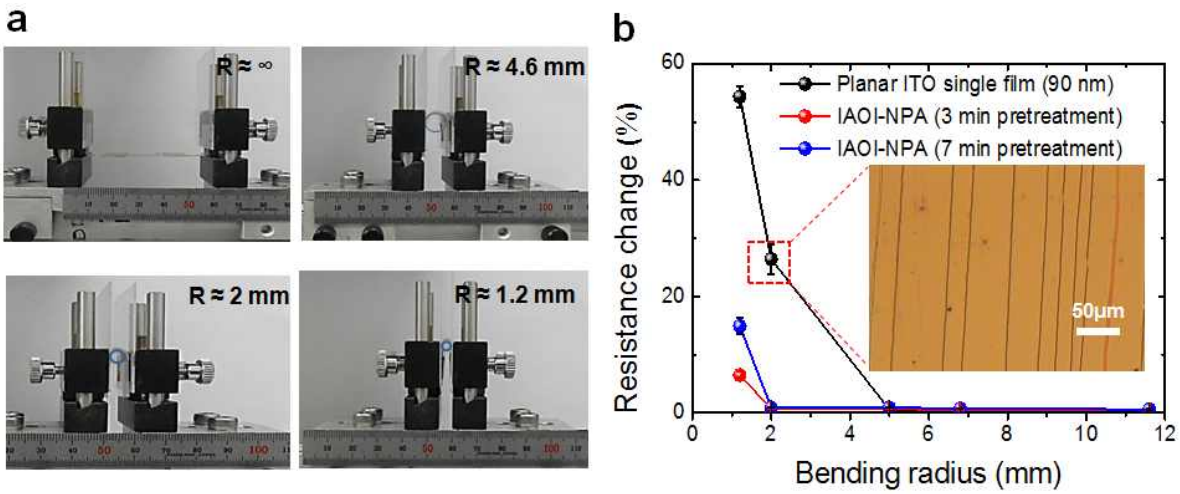

Fig. 10 (a) Photographs of the different electrodes being subjected to bending tests: 90-nm-thick planar ITO film, IAOI-NPA (3 min), and IAOI-NPA (7 min) electrodes. (b) The percentage change in the resistances of the electrodes as a function of the bending radius. The inset shows that cracks developed in the planar ITO film after being bent with a bending radius of 2 mm.

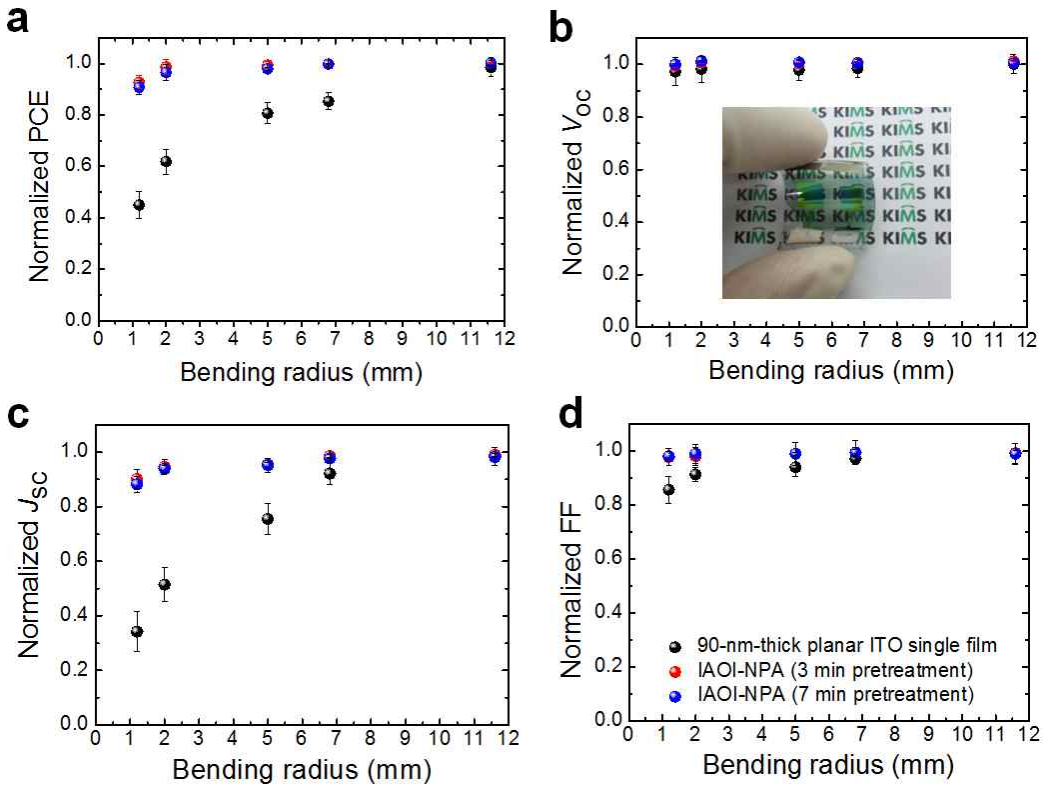

Fig. 11 Changes in (a) PCE, (b) V_{oc}, (c) J_{sc}, and (d) FF values of the flexible OSCs based on the photoactive polymer (PBDTTT-C:$PC_{61}BM$) in dependence of the bending radius during compressive bending of the PET substrates. The inset shows a photograph of a flexible OSC based on the IAOI-NPA electrode.

PTB-7:$PC_{71}BM$ as photoactive polymer layer. The OSC based on the IAOI-NPA (3 min) electrode exhibited an average PCE of 6.74 ± 0.05%, a record high value, with further improvements in the performance parameters, whereas the OSCs based on the planar ITO film and IAOI-NPA (7 min) electrodes exhibited lower average PCEs of 6.05 ± 0.06% and 5.63 ± 0.35%, respectively (Table 1). Efficient hole transport and separation, as well as the absence of a leakage current, were achieved in the OSC based on the IAOI-NPA (3 min) electrode and the PTB-7:$PC_{71}BM$ photoactive polymer. As a result, the J_{sc} and FF values of this OSC were dramatically improved to 14.58 ± 0.17 mA·cm^{-2} and 62.41 ± 0.81%, respectively. To our knowledge, a PCE of 6.74% is one of the highest values reported for flexible OSCs fabricated on polymer substrates and is even comparable to that of OSCs fabricated on glass.

That the IAOI-NPA electrodes are highly suited for use in OSCs is further proven by the fact that the electrodes exhibited stable conductivities even when subjected to a high degree of bending (Fig. 10). This was unachievable by use of planar ITO film-based electrodes. The changes in sheet resistance of the examined electrodes were measured by exposing the electrodes to compressive stresses, which were induced by subjecting the PET substrates to bending with successively decreasing radii (Fig. 10a). The percentage changes in the electrode resistances were determined for different bending radii. It was found that the resistance changes of the IAOI-NPA electrodes remained very stable even after the bending radius (R) was decreased to 2 mm, corresponding to a bending strain (ε) of 1.9% on the basis of the following relation, $\varepsilon = h_s/(2R)$, where h_s is the thickness of the PET substrate and R is the bending radius.[55] On the other hand, the planar ITO film-based electrode exhibited a dramatic increase in sheet resistance once the R value was less than 5 mm. Its sheet resistance increased by approximately 26% from its initial value at R = 2 mm. This was owing to the rapid development and propagation of microcracks, as shown in the inset (Fig. 10b). When the mechanical flexibilities of the OSCs were examined, the high flexibilities of the IAOI-NPA electrodes matched with the superior structural durabilities of the OSCs, based on these electrodes. Changes in the performance parameters of the OSCs, including their PCE, V_{oc}, J_{sc}, and FF values, for successively decreasing bending radii were tracked (Fig. 11). A decrease in J_{sc} and, thus, in the PCE value of the OSCs that are based on the IAOI-NPA electrodes, caused by the structural failure of the electrodes under bending, were not observed until the OSCs were bent with a radius as small as 1.2 mm. The performances of these OSCs remained stable against extreme bending, with the OSCs retaining more than 90% of their initial J_{sc} and PCE values. However, a similar behaviour was not observed in the OSC that is based on the planar ITO film-based electrode, which exhibited severe degradation in device performance for bending radii smaller than 7 mm. These results indicated that the use of IAOI-NPA electrodes results in completely foldable OSCs on polymer

substrates. It has been proven that such OSCs are difficult to realize using conventional film-type electrodes.

Conclusions

We have proposed a unique 3D nanoparticle-based electrode for OSCs built directly on heat-sensitive polymer substrates. Such electrodes are not realizable using conventional high-temperature vapor–liquid–solid or post-deposition sintering processes that are commonly employed for the fabrication of 3D nanorod-based electrodes on glass. The proposed IAOI-NPA electrode, which had a hybrid structure consisting of globular ITO nanoparticles superimposed on a continuous IAOI film, was fabricated on a PET substrate via plasma-induced polymer pre-treatment and subsequent room-temperature sputtering processes. The fabrication of the IAOI-NPA electrode is based on the self-assembly of ITO nanoparticles in precisely controllable dimensions and periodicity on the polymer surface. The high surface area of the electrode, which can be attributed to its nanoparticle-based geometry, and its low effective series resistance promoted charge transport and separation in corresponding OSCs. A high PCE of 6.74% was achieved in these OSCs, which were also completely foldable. This is an improvement of 11–22% against the PCEs of OSCs that use conventional planar ITO film-based electrodes.

Acknowledgements

This work was funded by the World Premier Materials (WPM) program as well as internal grants from the Korea Institute of Materials Science. W. Wang thanks the China Scholarship Council for financial support. The authors thank Y. Hwang of the Electronics and Telecommunications Research Institute (ERI) for her help with the XPS measurements and Dr. S. G. Lee of the Korea Basic Science Institute (KBSI) for his help with the XRD analyses.

Notes and references

[a] Key Laboratory for Liquid-Solid Structural Evolution and Processing of Materials, Shandong University, Jinan 250061, China.
[b] Surface Technology Division, Korea Institute of Materials Science, Changwon, Gyeongnam 641-831, Republic of Korea.
Fax: +82-55-280-3570; Tel: +82-55-280-3515;
E-mail: jungheum@kims.re.kr, smk1017@kims.re.kr.
[c] Jeonju Center, Korea Basic Science Institute, Jeonju, Jeonbuk 561-180, Republic of Korea.

† Electronic Supplementary Information (ESI) available: [FE-SEM images of Ar plasma-treated PET surfaces, Curve deconvolution of XPS Ag $3d_{5/2}$ spectra, Refractive indices and extinction coefficients of the Ag and AgO_x (O/Ag = 10 at%), Changes in the specular reflections of the IAOI-NPA and IAI-NPA electrodes for different O/Ag atomic ratios and thicknesses of the AgO_x layer, and Comparisons between the Jsc values determined from simulated AM1.5G illuminations and IPCE spectra.]. See DOI: 10.1039/b000000x/

1 W. U. Huynh, J. J. Dittmer, A. P. Alivisatos, *Science* **2002**, *295*, 2425.
2 W. Ma, C. Yang, X. Gong, K. Lee, A. J. Heeger, *Adv. Funct. Mater.* **2005**, *15*, 1617.
3 R. Yan, D. Gargas, P. Yang, *Nat. Photonics* **2009**, *3*, 569.
4 C. Cheng, H. J. Fan, *Nano Today* **2012**, *7*, 327.
5 K. M. Coakley, M. D. McGehee, *Appl. Phys. Lett.* **2003**, *83*, 3380.
6 K. M. Coakley, Y. Liu, M. D. McGehee, K. L. Frindell, G. D. Stucky, *Adv. Funct. Mater.* **2003**, *13*, 301.
7 W.-H. Baek, I. Seo, T.-S. Yoon, H. H. Lee, C. M. Yun, Y.-S. Kim, *Sol. Energ. Mat. Sol. C.* **2009**, *93*, 1587.
8 P.-C. Tseng, M.-H. Hsu, M.-A. Tsai, C.-W. Chu, H.-C. Kuo, *Org. Electron.* **2011**, *12*, 886.
9 D. C. Olson, J. Piris, R. T. Collins, S. E. Shaheen, D. S. Ginley, *Thin Solid Films* **2006**, *496*, 26.
10 Q. Wei, K. Hirota, K. Tajima, K. Hashimoto, *Chem. Mater.* **2006**, *18*, 5080.
11 P. Ravirajan, A. M. Peiró, M. K. Nazeeruddin, M. Graetzel, D. D. C. Bradly, J. R. Durrant, J. Nelson, *J. Phys. Chem. B* **2006**, *110*, 7635.
12 L. E. Greene, M. Law, B. D. Yuhas, P. Yang, *J. Phys. Chem. C* **2007**, *111*, 18451.
13 Y.-Y. Lin, C.-W. Chen, T.-H. Chu, W.-F. Su, C.-C. Lin, C.-H. Ku, J.-J. Wu, C.-H. Chen, *J. Mater. Chem.* **2007**, *17*, 4571.
14 H. K. Yu, W. J. Dong, G. H. Jung, J.-L. Lee, *ACS Nano* **2011**, *5*, 8026.
15 S. A. Choulis, J. Nelson, Y. Kim, D. Poplavskyy, T. Kreouzis, J. R. Durrant, D. D. C. Bradley, *Appl. Phys. Lett.* **2003**, *83*, 3812.
16 V. D. Mihailetchi, H. Xie, B. de Boer, L. J. A. Koster, P. W. M. Blom, *Adv. Funct. Mater.* **2006**, *16*, 699.
17 M. J. Bierman, S. Jin, *Energy Environ. Sci.* **2009**, *2*, 1050.
18 R. S. Wagner, W. C. Ellis, *Appl. Phys. Lett*. **1964**, *4*, 89.
19 Q. Wan, E. N. Dattoli, W. Y. Fung, W. Guo, Y. Chen, X. Pan, W. Lu, *Nano Lett*. **2006**, *6*, 2909.
20 A. J. Chiquito, A. J. C. Lanfredi, E. R. Leite, *J. Phys. D: Appl. Phys*. **2008**, *41*, 045106.
21 C. O'Dwyer, M. Szachowicz, G. Visimberga, V. Lavayen, S. B. Newcomb, C. M. Sotomayor Torres, *Nat*. *Nanotechnol*. **2009**, *4*, 239.
22 R. Savu, E. Joanni, *Scripta Mater*. **2006**, *55*, 979.
23 E. N. Dattoli, W. Lu, *MRS Bull.* **2011**, *36*, 782.
24 H. K. Yu, S. Kim, B. Koo, G. H. Jung, B. Lee, J. Ham, J.-L. Lee, *Nanoscale* **2012**, *4*, 6831.
25 M. M. Munir, F. Iskandar, K. M. Yun, K. Okuyama, M. Abdullah, *Nanotechnology* **2008**, *19*, 145603.
26 H.-W. Wang, C.-F. Ting, M.-K. Hung, C.-H. Chiou, Y.-L. Liu, Z. Liu, K. R. Ratinac, S. P. Ringer, *Nanotechnology* **2009**, *20*, 055601.
27 N. I. Kovtyukhova, T. E. Mallouk, *Nanoscale* **2011**, *3*, 1541.
28 Z. Yin, S. Wu, Z. Zhou, Z. Huang, Q. Zhang, F. Boey, H. Zhang, *Small* **2010**, *6*, 307.
29 N. P. Sergeant, A. Hadipour, B. Niesen, D. Cheyns, P. Heremans, P. Peumans, B. P. Rand, *Adv*. *Mater*. **2012**, *24*, 728.
30 W. J. Silva, H. P. Kim, A. Yusoff, J. Jang, *Nanoscale* **2013**, *5*, 9324.
31 R. Zhou, Y. Zheng, L. Qian, Y. Yang, P. H. Holloway, J. Xue, *Nanoscale* **2012**, *4*, 3507.
32 J. H. Lee, S. Cho, A. Roy, H.-T. Jung, A. J. Heeger, *Appl*. *Phys*. *Lett*. **2010**, *96*, 163303.
33 M. Dadu, A. Kapoor, K. N. Tripathi, *Sol*. *Energ*. *Mat*. *Sol*. *C*. **2002**, *71*, 213.

34 U. Schulz, P. Munzert, R. Leitel, I. Wendling, N. Kaiser, A. Tünnermann, *Opt. Express* **2007**, *15*, 13108.
35 B. Gupta, J. Hilborn, Ch. Hollenstein, C. J. G. Plummer, R. Houriet, N. Xanthopoulos, *J. Appl. Polym. Sci.* **2000**, *78*, 1083.
36 M. Collaud Coen, R. Lehmann, P. Groening, L. Schlapbach, *Appl. Surf. Sci.* **2003**, *207*, 276.
37 C. H. Bichler, H.-C. Langowski, U. Moosheimer, B. Seifert, *J. Adhes. Sci. Technol.* **1997**, *11*, 233.
38 S. Weidner, G. Kühn, R. Decker, D. Roessner, J. Friedrich, *J. Polym. Sci., Part A: Polym. Chem.* **1998**, *36*, 1639.
39 Q. T. Le, J. J. Pireaux, R. Caudano, P. Leclere, R. Lazzaroni, *J. Adhes. Sci. Technol.* **1998**, *12*, 999.
40 J. Yun, T.-S. Bae, S. Lee, S. Lee, J. Rha, G.-H. Lee, *Plasma Process. Polym.* **2012**, *9*, 135.
41 J. Yun, S. Lee, T.-S. Bae, Y. Yun, S. Lee, J.-D. Kwon, G.-H. Lee, *Plasma Process. Polym.* **2011**, *8*, 815.
42 J. Yun, T.-S. Bae, J.-D. Kwon, S. Lee, G.-H. Lee, *Nanoscale* **2012**, *4*, 7221.
43 J. Yun, Y. H. Park, T.-S. Bae, S. Lee, G.-H. Lee, *ACS Appl. Mater. Interfaces* **2013**, *5*, 164.
44 C. Guillén, J. Herrero, *Thin Solid Films* **2011**, *520*, 1.
45 K. Yvon, A. Bezinge, P. Tissot, P. Fischer, *J. Solid State Chem.* **1986**, *65*, 225.
46 R. W. G. Wyckoff, *Amer. J. Sci.* **1922**, *3*, 184.
47 L. H. Tjeng, M. B. J. Meinders, J. van Elp, J. Ghijsen, G. A. Sawatzky, R. L. Johnson, *Phys. Rev. B* **1990**, *41*, 3190.
48 J. F. Weaver, G. B. Hoflund, *J. Phys. Chem.* **1994**, *98*, 8519.
49 Y. Chiu, U. Rambabu, M. Hsu, H. Shieh, C. Y. Chin, H. H. Lin, *J. Appl. Phys.* **2003**, *94*, 1996.
50 A. I. Boronin, S. V. Koscheev, K. T. Murzakhmetov, V. I. Avdeev, G. M. Zhidomirov, *Appl. Phys. Sci.* **2000**, *165*, 9.
51 M. Bielmann, P. Schwaller, P. Ruffieux, O. Gröning, L. Schlapbach, P. Gröning, *Phys. Rev. B* **2002**, *65*, 235431.
52 Refractive Index Database, http://refractiveindex.info (accessed 07, 2013).
53 V. D. Mihailetchi, P. W. M. Blom, J. C. Hummelen, M. T. Rispens, *J. Appl. Phys.* **2003**, *94*, 6849.
54 A. Moliton, J.-M. Nunzi, *Polym. Int.* **2006**, *55*, 583.
55 S. I. Park, J. H. Ahn, X. Feng, S. Wang, Y. J. Huang, A. Rogers, *Adv. Funct. Mater.* **2008**, *18*, 2673.

A highly efficient 3D transparent conducting electrode is achieved by fabricating a multilayer consisting of an ITO nanoparticle array superimposed on an ITO–AgO_x–ITO electrode on a flexible polymer substrate by a room-temperature sputtering process. The high charge separation efficiency of the transparent 3D electrode facilitates a record high power conversion efficiency of 6.74% of a corresponding and mechanically foldable OSC.